Attributing Increases in Ozone to Accelerated Oxidation of Volatile Organic Compounds at Reduced Nitrogen Oxides Concentrations

Zekun Zhang[a], Jiakui Jiang[a], Bingqing Lu[a], Xue Meng[a], Hartmut Herrmann [ID][c], Jianmin Chen [ID][a] and Xiang Li [ID][a,b,*]

[a]Department of Environmental Science & Engineering, Fudan University, Shanghai 200032, China
[b]Institute of Eco-Chongming (IEC), Shanghai, China
[c]Leibniz-Institut für Troposphärenforschung (IfT), Permoserstr. 15, 04318 Leipzig, Germany
*To whom correspondence should be addressed: Email: lixiang@fudan.edu.cn
Edited By: Jiahua Zhang

Abstract

Surface ozone (O_3) is an important secondary pollutant affecting climate change and air quality in the atmosphere. Observations during the COVID-19 lockdown in urban China show that the co-abatement of nitrogen oxides (NO_x) and volatile organic compounds (VOCs) caused winter ground-level O_3 increases, but the chemical mechanisms involved are unclear. Here we report field observations in the Shanghai lockdown that reveals increasing photochemical formation of O_3 from VOC oxidation with decreasing NO_x. Analyses of the VOC profiles and NO/NO_2 indicate that the O_3 increases by the NO_x reduction counteracted the O_3 decreases through the VOC emission reduction in the VOC-limited region, and this may have been the main mechanism for this net O_3 increase. The mechanism may have involved accelerated OH–HO_2–RO_2 radical cycling. The NO_x reductions for increasing O_3 production could explain why O_3 increased from 2014 to 2020 in response to NO_x emission reduction even as VOC emissions have essentially remained unchanged. Model simulations suggest that aggressive VOC abatement, particularly for alkenes and aromatics, should help reverse the long-term O_3 increase under current NO_x abatement conditions.

Keywords: ozone; VOCs and NO_x reduction ; photochemical box model

Significance Statement:

Tropospheric O_3 is an important secondary pollutant affecting climate change and air quality in the atmosphere. However, its response to precursor emission reductions is unclear. It is generally assumed to depend on the levels of NO_x and VOC reductions. However, we show here that the fast oxidation of VOCs occurs at decreased NO_x emissions during Shanghai's COVID-19 lockdown and can explain the substantial net O_3 increase. This could explain why O_3 has increased in response to NO_x emission reduction even as VOC emissions have remained unchanged. The mechanism may involve accelerated OH–HO_2–RO_2 radical cycling.

Introduction

Ground-level ozone (O_3) is an air pollutant detrimental both to human health (1) and to terrestrial vegetation (2). In the mid-20th century, Haagen-Smit et al. proved that O_3 is generated by the photochemical reaction of volatile organic compounds (VOCs) and nitrogen oxides(NO_x) in sunlight (3). It is now well established that the chemistry of O_3 formation is highly nonlinear and pertains to the coupling of the "NO_x cycle" and the "RO_X ($RO_X = OH + HO_2 + RO_2$) radical cycle" (4–6). The NO_x and RO_X cycles are terminated by the cross-reaction of NO_x and/or RO_X. From the perspective of O_3 pollution reduction, if HO_2 self-reaction and its reaction with RO_2 constitute the dominant termination reaction (known as the "NO_x-limited" regime), reductions in NO_x emissions serve the greatest benefit. Meanwhile, if the reactions of NO_2 with OH and RO_2 form the dominant termination reaction (known as the "VOC-limited" regime), reductions in VOC emissions prove
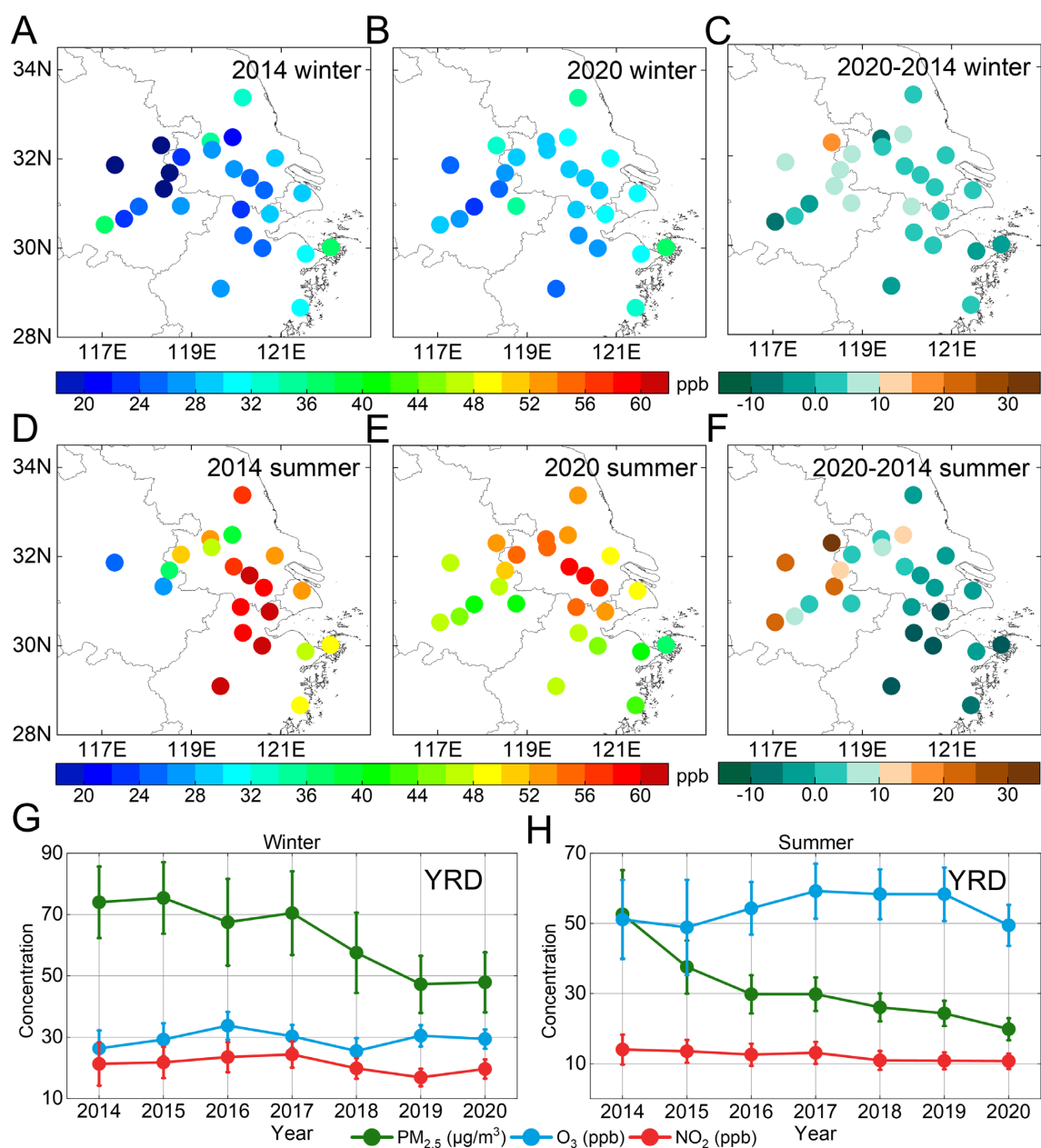
the most effective (5, 7). In the context of China, most city clusters [e.g. the Pearl River Delta, Yangtze River Delta (YRD) and Northern China Plain] are found to be VOC-limited (5), with anthropogenic VOCs dominating, whereas most rural areas are NO_x-limited in this regard (8).

China has been confronting serious air pollution for several years (9, 10). In an attempt to improve air quality, China has implemented strict pollution control policies since 2013. However, ground-level O_3 concentrations have not improved following NO_x abatement (11, 12). Recent studies have shown that VOCs and NO_x should be controlled simultaneously to reverse O_3 increases (13, 14). These results concur with those of Pusede (15) and Roberts et al. (16), who found that simultaneous VOC and NO_x abatement could considerably mitigate the peak of O_3 production and prevent surface air quality deterioration.

Fig. 1. Variations in winter and summer YRD's MDA8 O_3 concentrations from 2014 to 2020. (A and B) Distributions of winter mean MDA8 O_3 concentrations in YRD in 2014 and 2020. (D and E) Distributions of summer mean MDA8 O_3 concentrations in YRD in 2014 and 2020. (C and F) Reductions of winter and summer mean MDA8 O_3 concentrations between 2014 and 2020 (negative values). (G and H) Interannual variation (Error bars: SD) of NO_2, MDA8 O_3 and $PM_{2.5}$ in the YRD during winter and summer.

The large-scale emission reductions seen during the COVID-19 lockdown are unprecedented opportunities for improving our understanding of O_3's response to the control of its precursor emissions. The Chinese government adopted countrywide measures from January 23 to February 13, 2020, to prevent the propagation of the disease. According to satellite and surface observations, NO_2 concentrations in China decreased by >50% during the lockdown period compared with those in the pre-lockdown period, and other pollutants such as $PM_{2.5}$ and CO also decreased significantly [17–19]. However, ground-level O_3 concentrations in parts of China increased substantially [20–22]. The increase in O_3 during the lockdown has been tentatively attributed to weakened titration [23, 24], O_3 production [25], and decreased $PM_{2.5}$ [19, 24].

However, the changes in the chemical mechanisms connecting O_3 levels with the abatement of its precursors are rarely discussed.

Here, we use detailed field observations during the Shanghai lockdown combined with an observation-based model (OBM) to show evidence for the increased photochemical formation of O_3 from VOC oxidation with decreasing NO_x. We demonstrate that this mechanism can explain the observed O_3 increase. This also helps explain why O_3 concentrations in China increased in recent years as NO_x emissions have greatly decreased while VOC emissions have remained unchanged [26, 27]. We further show that a reasonable ratio of annual NO_x and VOC reduction decreases O_3 photochemical production, with important implications for developing O_3 pollutant control strategies to decrease O_3 in China.
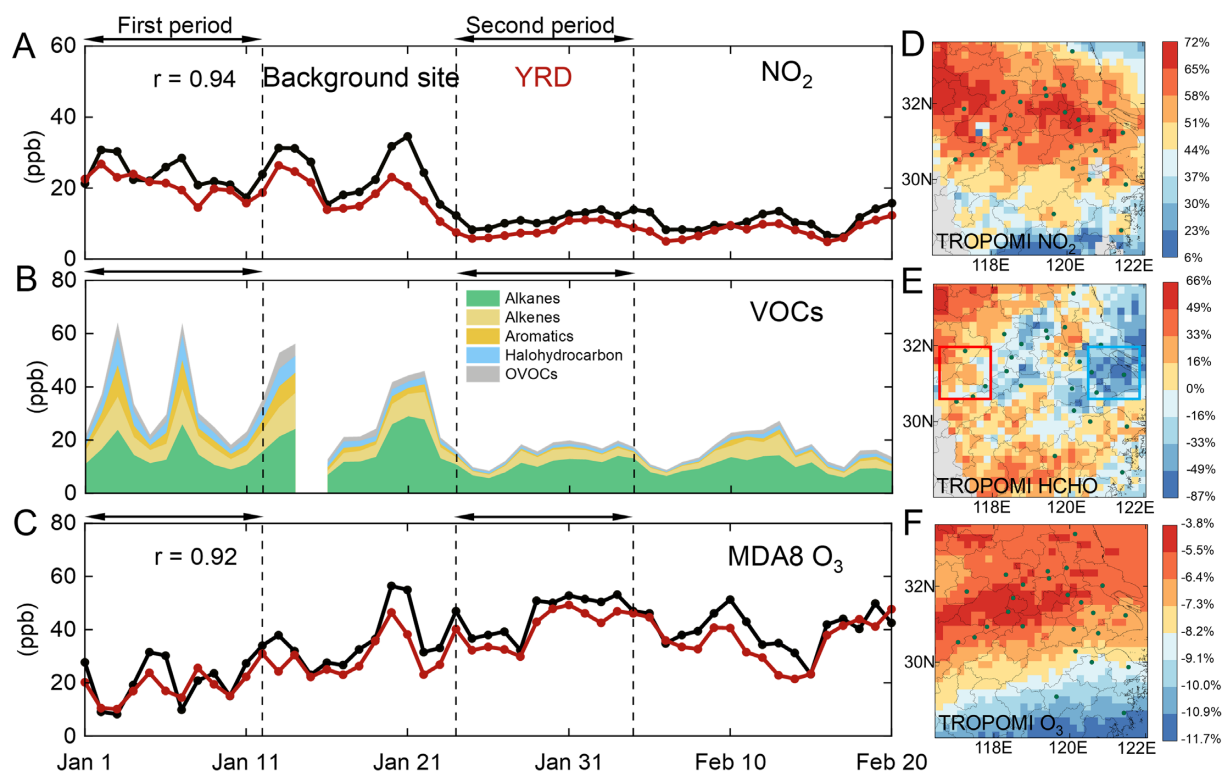
Fig. 2. Air quality changes in YRD in response to the COVID-19 lockdown from January 1 to February 20, 2020. (A and C) The red lines show observed concentrations of 24-h average NO₂ and MDA8 O₃ at YRD. The NO₂ and O₃ observations are averages across the monitoring sites of the MEE. Also shown are observations results sampled at the background site and the corresponding correlation coefficients (*r*). (B) VOCs observation data from background site. (D, E, and F) Relative percentage change [(FP-SP)/FP] in tropospheric NO₂, HCHO, and O₃ column densities measured by the TROPOMI satellite instrument during FP and SP. The TROPOMI aggregation is on a 5.5 × 3.5 km grid.

Results and Discussion
Worsening O$_3$ air quality from 2014 to 2020

Fig. 1A to F shows the spatial distribution of the winter and summer mean maximum daily 8-h average O$_3$ (MDA8 O$_3$) concentrations around the YRD (Figure S1) in 2014 and 2020 (maps for 2015 to 2019 are presented in the Figure S2). In both years, high levels of MDA8 O$_3$ concentrations were observed in the eastern YRD, especially in Shanghai and surrounding regions, where the emission intensity was the highest (28). As illustrated in Fig. 1C and F, a slight increase in MDA8 O$_3$ concentrations occurred across the YRD from 2014 to 2020 even with considerable reductions in the emissions of major air pollutants (Figures S3 and S4, and Tables S1 to S3). According to an estimate of the temporal trend (Fig. 1G and H), the winter (summer) YRD concentration of MDA8 O$_3$ increased by 0.43% yr^{-1} (1.25% yr^{-1}) from 2014 to 2020. The titration effect caused by the 2.3% yr^{-1} (4.1% yr^{-1}) NO$_x$ decreases along with unchanged VOCs was found to be a significant cause of such increases. Meanwhile, the 6.2% yr^{-1} (9.2% yr^{-1}) reductions in PM$_{2.5}$ may also be major factors as aerosol particles scavenge hydrogen oxide (HO$_x$) and nitrogen trioxide (NO$_3$) radicals, which would otherwise produce O$_3$ (29). Similar increases in O$_3$ simultaneously recorded with the progressive implementation of clean-air actions were generally observed in various areas of China, including the North China Plain and Pearl River Delta (30, 31). Such results point to potential increases in oxidation capacity in the YRD. Although NO$_x$ reduction has traditionally been considered important for controlling O$_3$, recent studies have shown that the co-abatement of VOCs and NO$_x$ is more important for suppressing O$_3$ photochemical production (32, 33). In this regard, COVID-

19 represents an opportunity that informs our understanding of how VOCs and NO$_x$ should be effectively controlled to reverse O$_3$ increases.

The national lockdown policy in response to COVID-19 beginning on 2020 January 24, impelled a rapid drop in transportation and industrial emissions, compounded by the Chinese Spring Festival holiday (19, 34). For the present work, the "first period" (FP) comprised the normal emissions from January 1 to January 11, and the "second period" (SP) included the lockdown from January 24 to February 3 when lockdown restrictions were at their height (34). Fig. 2 and Figure S5A show 40% to 80% observed decreases in surface NO$_2$ levels and tropospheric NO$_2$ columns from the TROPOspheric Monitoring Instrument (TROPOMI) satellite, suggesting rapid falls in NO$_x$ emissions in the YRD (the measurement of sites changes are discussed in SI Appendix A, Figure S6 and S7, and Tables S4 to S7). TROPOMI Formaldehyde (HCHO) observations suggest a weaker reduction in VOC emissions (Fig. 2E). For example, TROPOMI HCHO decreased by 12% in the western YRD (red squares), whereas it increased by 38% in the eastern area (blue squares). The surface NO$_2$ concentrations came from the Ministry of Ecology and the Environment (MEE) monitoring site network. For the eastern YRD, as laid out in Fig. 2E, the average falls in the course of SP were 40% for surface NO$_2$ and 60% for TROPOMI NO$_2$. Conversely, the O$_3$ concentrations quantified at MEE sites and TROPOMI satellite increased in the course of the SP (Figure S6B and Fig. 2F). Ground-level MDA8 O$_3$ in the YRD increased from 18 ± 5 ppb during the FP to 40 ± 5 ppb during the SP.

We utilized a machine learning model to predict O$_3$ levels in a "business-as-usual" scenario (Materials and Methods section).

Figure S8 shows that the O_3 concentration during the lockdown significantly increased compared with that in the business-as-usual scenario. The increase in O_3 might well be explained by unfavorable meteorological conditions and the co-abatement of O_3 precursors. Therefore, we prioritized the use of multiple linear regression (MLR) models to assess the meteorological short-term effects on MDA8 O_3 before and after the lockdown (2020 January 1 to 2020 February 29) in the YRD (35). The coefficient of determination (R^2), for the MLR model in fitting MDA8 O_3 anomalies in the YRD was 0.52 (regression coefficients are summarized in Table S8). We then used the Lindeman, Merenda, and Gold method to quantify the relative importance of each meteorological variable in explaining that the atmosphere-driven O_3 increases (Figure S9). A decrease in fractional total cloud cover during the lockdown (Table S9) was the most significant driver of the O_3 increase seen in the YRD with a contribution of 41%. Less cloud cover favors strong solar radiation, which in turn promotes O_3 production (36). We found that 850-hPa relative humidity (RH850) was negatively correlated with O_3 (regression coefficient: −0.3) because wet aerosols formed under high humidity reduce ultraviolet actinic flux and thereby inhibit photochemical reaction rates (37). Meanwhile, the weakening of the 10-m zonal wind (U10, 7%) and 10-m meridional wind (V10, 3%) caused less downwind flux of O_3, resulting in more O_3 remaining *in situ* in the YRD (Table S9) (38). These findings further demonstrated the importance of meteorological short-term effects on O_3 (39). However, VOC and NO_x reduction effects on O_3 formation mechanisms must be further considered to effectively understand the impact of the lockdown on O_3 production.

Evidence for O_3 formation by accelerated photochemistry

The cycle between OH and HO_2 is highly pertinent to O_3 formation, influencing the chain reaction propagation (40). Thus, the levels and reaction routes of free radicals are significant factors in O_3 generation. The simulated diurnal patterns (3-day average) of free radicals at urban and background sites are displayed in Fig. 3A and B, and Figure S10A and B. The highest levels of free radicals were modeled around 12:00 to 13:00 at two sites. The daily peak of OH at the urban site increased by ~0.69× 10^6 cm^{-3} in the SP relative to the FP but decreased by 0.86 × 10^6 cm^{-3} at the background site. Meanwhile, the daytime-averaged OH concentration (08:00 to 16:00) at the urban site (0.89 × 10^6 cm^{-3}) was comparable with that at the background site (0.67 × 10^6 cm^{-3}) during the SP. The daytime-averaged OH level simulated in this research was comparable with that (1.5 ± 0.9 × 10^6 cm^{-3}), modeled on a Beijing winter (41).

In comparison, the daily peak of HO_2 at the urban site increased by ~0.95 × 10^7 cm^{-3} but decreased by 0.49 × 10^7 cm^{-3} at the background site. The daytime-averaged HO_2 concentration at the background site (1.02 × 10^7 cm^{-3}) during the FP was more than double that at the urban site (0.41 × 10^7 cm^{-3}), whereas the HO_2 concentrations were similar at both sites during the SP, which was more likely because there were less VOCs at the background site and thus less HO_2 produced through photochemical reactions. The daytime-averaged HO_2 concentration at both sites during the SP was higher than that (0.52 ± 0.23 × 10^8 cm^{-3}) in Beijing during typical winter pollution episodes (the atmospheric oxidation capacity and the OH reactivity are discussed in SI Appendix B and Figures S11 and S12) (42). Table S10 compares the OH and HO_2 levels for different Chinese cities. The differing levels of free radicals in various studies may be attributed to the different air pollutants and weather conditions at each locale sampled (40). The peak OH and

HO_2 concentrations responded differently at the two sites, highlighting the complex effects of the levels of NO_x and VOC reductions on photochemistry (23, 43).

Because OH–HO_2–RO_2 is to a great extent responsible for the oxidation capacity of the atmosphere, calculating its radical sources and sinks offers an insightful understanding of the effects of the co-abatement of NO_x and VOCs on atmospheric chemical processes. The average production and loss rates for OH–HO_2–RO_2 radicals at the urban and background sites are shown in Fig. 3C and D, and Figure S10C to D. The reaction HO_2 + NO was the main OH production source, with reaction rates reaching 1.27 and 2.71 ppb h^{-1} for urban and background sites during the FP, respectively. However, this reaction increased to 1.67 ppb h^{-1} at the urban site and decreased to 0.84 ppb h^{-1} at the background site during the SP. Next, came the photolysis of HONO. The OH production rate from this reaction weakened by 48% and 66%, respectively, for the two sites. The main mechanism of OH consumption was the production of HNO_3 and HO_2. During the FP, the high OH + NO_2 reaction rate (to produce HNO_3) was for the most part due to the relatively high daily average NO_x level at the urban (39.1 ppb) and background (26.6 ppb) sites (44). With NO_x abatement, this reaction fell by 41% and 59% at the urban and background sites, respectively. Unlike the OH + NO_2 response, the rate of HO_2 production from OH rose by 57% at the urban site but fell by 58% at the background site during the SP, probably due to different levels of NO_x and VOC co-abatement in the two locations.

In addition to OH, RO and oxygenated VOCs (OVOCs) were also primary sources of HO_2. These two chemical pathways decreased by 18% and 32%, respectively, at the urban site during the SP but decreased by 73% and 74%, respectively, at the background site. The major HO_2 removal mechanism was its reduction reaction with NO, which produced OH radicals. Some research has also revealed that HO_2 radicals can be taken up by aerosols (45). The RO_2 formation rates of OH and OVOCs did not change significantly for the urban site but decreased by 36% and 67%, respectively, at the background site. Substantial VOCs reductions are important factors in the decline of the background site RO_2 formation rates. We keenly point out that the reactions NO + HO_2 and RO_2 + NO are the two major pathways for radical cycling at the two sites during the FP and SP, which are common in NO_x-rich environments (46, 47). Obviously, our results show that the OH–HO_2–RO_2 cycling at urban stations remained at high levels during the lockdown, with particularly enhanced cycling between OH and HO_2. Meanwhile, significant weakening was observed at the background sites, which may have depended on the levels of VOC abatement.

We further examined the O_3 formation mechanisms for the lockdown. O_3 was mainly produced through the oxidation of NO by HO_2 and RO_2 (48). For the O_3 loss, the predominant scavenging pathways were the photolysis of O_3 and the NO_2 + OH reaction. Fig. 3E and F, and Figure S10E and F show the detailed O_3 chemical budgets before and after the lockdown at the urban and background sites. The major photochemical production of O_3 was clearly demonstrated, with net daytime O_3 average generation rates of 1.5 and 3.8 ppb h^{-1} for the urban and background sites, respectively, during the FP. The O_3 production intensity at the two sites was lower than that derived from an urban site in Wuhan autumn (8.8 ppb h^{-1}) (44) and comparable with that in Beijing's clean episode (2 ppb h^{-1}) (41). During the SP, the net daytime O_3 average generation rates increased to 1.8 ppb h^{-1} for urban sites but decreased to 0.8 ppb h^{-1} for background sites. This may have had something to do with the O_3 production rate increase from
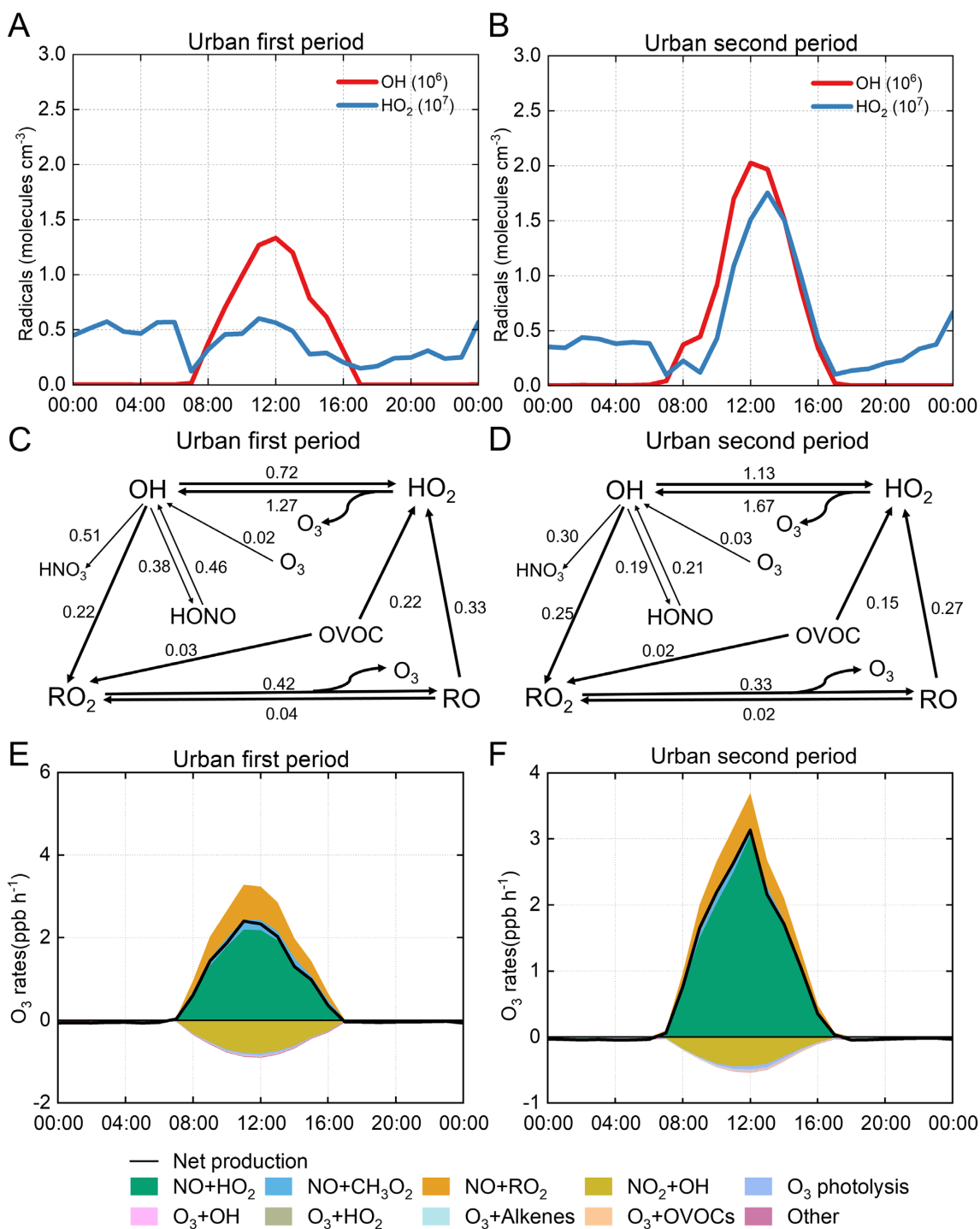
Fig. 3. Relevant simulation results (3-day averaged) for urban site during FP and SP. (A and B) Simulated average diurnal variations in OH and HO_2. (C and D) Daytime (08:00 to 16:00 LT) average OH-HO_2-RO_2 budget. Units: ppb h^{-1}. (E and F) Model-simulated average chemical budgets of O_3.

NO_x reduction exceeding the decrease rate associated with VOC reduction at urban sites, causing an increase in net O_3 production rate and, thus, a substantial O_3 increase (Figure S13A and B). Conversely, the NO_x reductions at the background sites had less impact on O_3 than the control of the VOCs, leading to the decrease in O_3 production rates (Figure S13C and D). The O_3 production rate peaks around midday (literally at around 12:00 LT), only to be succeeded by a major drop during the afternoon, consistent with the overall findings from other works that reported noon or afternoon peaks (49, 50).

The links between O_3 and precursor species are elucidated more by the relative incremental reactivity (RIR) process using the OBM (Materials and Methods section). As can be seen in Figure S14, the simulation results for the two sites were the same during the FP and SP. The RIR values of each VOC category were positive for all scenarios, and only NO_x was negative, indicating that O_3 formation was consistently in the VOC-limited regime (51). During the FP, the two sites had high RIR for aromatics and alkenes, which showed that they control the production of O_3 to a larger extent. Notably, we found that O_3 production at both sites was
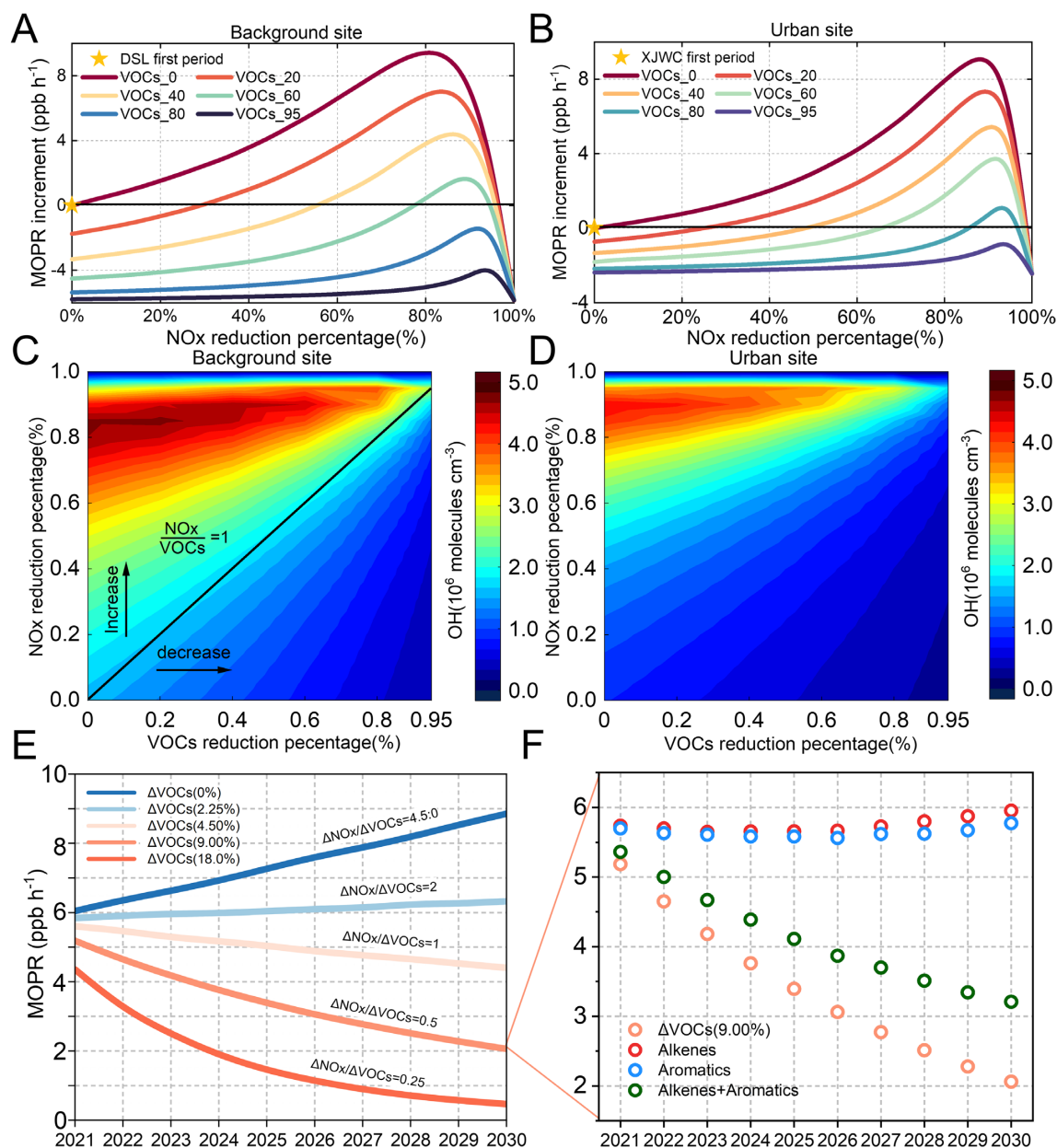
Fig. 4. Simulation in background and urban sites according to the emission changes of NO_x and VOCs, with first period (yellow pentagon) as the simulation scenario. (A and B) MOPR increment in background and urban site, the black line represents zero MOPR increment. (C and D) Isopleths of daytime OH concentration in background and urban sites. (E) In a 4.5% annual NOx reduction scenario, simulation of MOPR under five $\Delta NO_x/\Delta VOCs$ reduction ratios from 2021 to 2030. (F) MOPR is simulated for alkenes, aromatics, and alkenes and aromatics at an annual reduction rate of 9% for the scenario.

more sensitive to alkenes and CO during the SP, suggesting that future targets of O_3 control should emphasize reducing not only the active species of VOCs but also CO emissions.

Implications for air pollution control

O_3 formation was determined to be in the VOC-limited regime at the background and urban sites. However, how much VOCs should be controlled to achieve the optimal O_3 reduction was nonetheless uncertain, particularly in a future emission scenario where VOCs and NO_x tend to be controlled simultaneously. In the pursuit of this objective and to offer detailed information on the requisite decreases in VOCs and NO_x, we simulated the maximum O_3 production rate (MOPR) increment with the reduction of both VOCs and NO_x (Fig. 4A and B). We found that at the background (ur-

ban) site, when the mixing ratios of VOCs were lowered from 0% to 95%, the appropriate reduction percentages of NO_x tended to fall between 0% and 78% (85%) or in the range of 94% (96%) to 100% for the zero MOPR increment. Admittedly, reducing NO_x by 94% to 100% may prove impracticable. Therefore, this section looked primarily at the range 0% to 78% (85%) in NO_x reduction to produce the best possible VOC and NO_x control measures. The researchers found that the MOPR could be reduced when the NO_x/VOC co-abatement ratio was <1.5 for the background site, resulting in the suppression of O_3 production, and 1.25 for the urban site (i.e. the cutting ratios of $NO_x/VOCs$ where the curves meet the MOPR zero increment line). However, the simulation results for OH and HO_2 radicals at both sites showed that the radical concentrations can be effectively reduced when $NO_x/VOCs$ <1 (Fig. 4C and D and Fig-

ure S15). This indicates that the weakening of OH and HO_2 experiences lags relative to the MOPR, which may influence atmospheric $PM_{2.5}$ formation (52). Similar simulation results for the two sites indicate the consistency of future co-abatement strategies for Shanghai and the YRD.

We obtained a reasonable ratio above by controlling the total abatement of NO_x and VOCs. However, to achieve the National Ambient Air Quality Standard for O_3, NO_x and VOC emissions must be reduced to a large degree (14, 53), which cannot be accomplished in the short-term. Thus, reasonable annual reduction plans should be developed to ensure their enforceability. Accordingly, NO_x emissions are assumed to annually decrease by 4.5% ($\Delta NO_x = 4.5\%$). The reduction rate in NO_x was referenced to the trend of winter NO_2 concentration in Shanghai, Nanjing, Hangzhou, and the YRD region from 2014 to 2020 (Figure S16). Working with this postulate, we looked at the associated benefits of various VOC emission reduction rates for 2021 to 2030. As presented in Fig. 4E, we designed five control scenarios with different VOC control rates. For every scenario, the annual emission reduction rate was the same during the emission control period. The results show the additional lowering of the MOPR with faster VOC emission control than those under lower VOC falls. Taking the annual VOC reduction rates ($\Delta VOCs$) of 4.5%, 9%, and 18% as examples, the MOPR reduction rates were 4.5, 6.7, and 8.5 ppb h^{-1}, respectively, compared with the zero VOC reduction (0%) in 2030. Apparently, controlling VOCs to large extents can guarantee the effectiveness of NO_x control in lowering O_3. Such reduced O_3 levels arising from extensive VOC control strategies can introduce other positive effects through the reduction of their negative effects on humans and nature (14).

The above results indicate that the MOPR decreases yearly when annual $\Delta VOCs \geq 4.5\%$. Considering the lag of free radical decrease relative to MOPR (Figure S17) and economic feasibility, we considered annual $\Delta VOCs$ of 9% to be reasonable. Meanwhile, previous results showed that alkenes and aromatics have stronger control effects on O_3 formation. To highlight the role of reactive VOCs in future controls, we conducted sensitivity simulations by removing the effects of other VOCs (Fig. 4F). We found that the reduction of alkenes and aromatics alone can only offset the negative impact of NO_x reduction relative to zero VOC reduction conditions. For the condition with both reductions, we see from Fig. 4F that the weakening of MOPR is also significant relative to the condition with all VOCs reduced. This implies that future VOC plans should prioritize the reduction of alkenes and aromatics (54).

In summary, we have shown evidence from field observations in the Shanghai lockdown that reveal the increasing photochemical formation of O_3 from VOC oxidation under decreased NO_x emission to promote O_3 production. The evidence suggests that the O_3 increase by the NO_x reduction counteracted the O_3 decrease by the VOC emission reduction in the VOC-limited region. Therefore, O_3 control requires more aggressive VOC reduction under current NO_x reduction conditions, particularly for alkenes and aromatic VOCs. What we present thus explains the O_3 increase in the lockdown despite the reductions in its precursors. This also helps explain why O_3 has increased from 2014 to 2020 in response to NO_x emission reduction even as VOC emissions have remained unchanged. Although the national lockdowns are not sustainable, O_3 response to the precursor emission reductions could be used as a reference for future VOC and NO_x control. The reduction associated with O_3 formation may be important for aerosol climate effects and in understanding pollution–weather feedback loops, most particularly the mitigation of PM formation through VOC reduction (55, 56).

Materials and Methods
Observations

The YRD, located in eastern China adjacent to the East China Sea, is one of the biggest city conglomerates in the world. Its location places it in a subtropical monsoon climate. Although the YRD covers only about 1.1% of China's total land area, it is home to ~7.6% of China's total population and accounted for 16.5% of the country's Gross Domestic Product in 2016 (http://data.stats.gov.cn/). The high population density and widespread heavy industries lead to intensive energy consumption and emission of pollutants. Therefore, the YRD region has experienced severe O_3 pollution and is considered the key prevention and control area for O_3 pollution in China (57, 58). In this study, 26 cities in the YRD were considered (Figure S1A): Shanghai, Nanjing, Wuxi, Changzhou, Suzhou, Nantong, Yancheng, Yangzhou, Zhenjiang, Taizhou, Hangzhou, Ningbo, Jiaxing, Huzhou, Shaoxing, Jinhua, Zhoushan, Taizhou, Hefei, Wuhu, Maanshan, Tongling, Anqing, Chuzhou, Chizhou, and Xuancheng. The above data of routine air pollutants ($PM_{2.5}$, NO_2, CO, O_3) at ground level for winter (December, January, and February) and summer (June, July, and August) 2014 to 2020 in 26 cities were obtained from the China National Environmental Monitoring Center (CNEMC). Monitoring data were collected using continuous automated equipment. All equipment passed the applicability test by the CNEMC, and all monitoring data were subjected to validity audits.

The field experiment was conducted at the background (121.021°E, 31.238°N) and urban site (121.507°E, 31.329°N) in YRD region, China. The background site (Figure S1B) is surrounded by Dianshan Lake and several villages with low population density and is about 40 km away from the built-up center of Shanghai. The region is frequently defined as a reference for the study of air pollution in the YRD (59, 60). The urban site is surrounded by a concentration of residential areas, commercial areas, schools and hospitals, which was under strong influence by urban pollutant emissions.

At the background and urban observation sites, NO_x (NO/NO2) and 60 VOCs were measured. To be specific, hourly concentrations of 60 VOC species were monitored by an online gas chromatography analyzer (Focused Photonics, GC955-615), VOC species are detailed in Table S6. Ambient pollutants were monitored by Thermo Environmental Instruments. NO, NO_2, and NO_x were detected by the NO-NO_2-NO_x analyser (Model 42i). For routine gaseous pollutant concentration ($PM_{2.5}$, O_3, NO_2, SO_2, and CO) monitoring, we used monitoring data from the CNEMC sites nearest to the background and urban site. In addition, meteorological data (temperature, humidity, etc.) are collected hourly from the ERA5 reanalysis dataset.

Satellite observations of O_3, NO_2 and HCHO columns from the TROPOMI instrument were accessed from https://s5phub.copernicus.eu/dhus/. TROPOMI provides daily global coverage with 5.5×3.5 km^2 pixel resolution. TROPOMI data have been applied in tracking anthropogenic emission changes during the lockdown. In this study we used the TROPOMI level 2 observations (Table S11).

The LightGBM model

LightGBM is a state-of-the-art gradient-boosting framework that uses tree-based learning algorithms. It is designed with faster training speed, lower memory usage, better accuracy and capability of handling large-scale data (61). We trained the LightGBM model with 17 features and ozone labels from 1 January 2019 year to 23 January 2020 (Table S12). To achieve better performance, we performed grid tuning of the parameters by a randomly crossval-

idated search on parameter settings. We finally selected the following hyperparameters: max depth = 16, num estimators = 127, reg alpha = 5, learning rat = 0.1. Notably, the emission levels for the "business-as-usual" scenario in the model were calculated using the methodology of shi et al (25).

Observation-based model (OBM)

The OBM for the investigation of atmospheric oxidative capacity and photochemistry (OBM), as a zero-dimensional box model, has been extensively used to simulate atmosphere chemical processes (62–65). It is based on the latest version of the Master Chemical Mechanism (MCM v3.3.1) (66), which contains more than 5800 chemical species and 17 000 reactions, especially, over 200 reactions about VOCs oxidation by chlorine radical. Expect for gas-phase reactions, several heterogeneous processes and physical processes are considered in simulation (67, 68). However, the impact of changes in aerosol loading on HO_2 and O_3 production is not parameterized in the model. The latest study by lvatt et al. (45) shows that a novel "aerosol suppression" regime is suppressing surface O_3 production in China and suggests removing the uptake of HO_2 into aerosols increases O_3 concentrations in the North China Plain by 20% to 30%. This result is based on the 2014 emission scenario. $PM_{2.5}$ concentrations in the YRD region are significantly decreased in 2020 compared to 2014 (Fig. 1G and H), therefore we suggest that the sensitivity of surface O_3 to HO_2 uptake in China has currently been reduced. This is in line with lvatt et al., who consider that O_3 sensitivity to HO_2 uptake had reduced in Europe, North America and Japan as policy interventions had reduced particulate-matter concentrations.

In this study, we used the field-measured VOCs, O_3, NO, NO_2, SO_2, and CO, and physical parameters to constrain the boundary of the model and input them into the model for calculation. The photolysis frequencies data were obtained from the Tropospheric Ultraviolet and Visible (TUV, v5.3.1) model combined with the European Centre for Medium-Range Weather Forecasts (ECMWF) products ERA5 reanalysis dataset and observed data. Moreover, the missing VOCs data were interpolated using the MLR with other hour data of the day or average the close hour data. If the data miss more than three hours in a day, the average value of the corresponding hour during this period will represent the hourly value of that day.

OBM is able to simultaneously quantify the O_3 production rate, atmospheric oxidation capacity (AOC), OH reactivity, and the primary production, recycling, and termination rates of OH–HO_2–RO_2 radicals (62). Here, we focus on AOC, O_3 budget, and OH–HO_2–RO_2 budget. Before each simulation, the model starts at 00:00 LT and pre-run eight days under constraints of input data to reach a steady-state for unmeasured species in the sampling field.

Relative incremental reactivity (RIR)

The RIR is an important index to evaluate the sensitivity and control factors of ozone generation, which can also be calculated by OBM (69–71). The definition of RIR is the ratio of the percentage change in ozone formation rate to the percentage change in ozone specific precursor source strength after changing ozone specific precursor source strength, seeing equation.

$$RIR = \frac{[P_{O_3-NO}(X) - P_{O_3-NO}(X - \Delta X)]/P_{O_3-NO}(X)}{\Delta S(X)/S(X)}. \quad (1)$$

Where X represents either a specific precursor or a group of VOCs, ΔX is the hypothetical change of X (20% was adopted in this study). $P_{O_3-NO}(X)$ and $P_{O_3-NO}(X - \Delta X)$ mean the production rate

of simulated O_3 based on measured concentration and emission reduction concentration. S(X) and S(ΔX) are the concentration of these corresponding specific precursors and the hypothetical changed concentration, with the unit of per part billion.

Multiple linear regression (MLR)

We performed a stepwise MLR model applied to daily MDA8 O_3 concentrations by considering many candidate meteorological variables from the ERA5 reanalysis. The MLR model is in the following form:

$$y = \beta_0 + \sum_{k=1}^{10} \beta_k x_k + interaction\ terms, \quad (2)$$

where y is the daily MDA8 O_3 concentrations, and ($x_1,. . ., x_8$) are the eight meteorological variables (Table S8) that were selected by a stepwise method featuring the best model fit. All y and x_k data need to be normalized by subtracting the mean and dividing by the SD.

We next use the LMG (Lindeman, Merenda, and Gold) method to quantify the relative importance of each of the ten selected meteorological variables in explaining the atmospherically driven increase in O_3 in Shanghai over pre-lockdown and COVID-19 lockdown. The LMG method can divide the total R^2 explained by the MLR model into each non-negative individual R^2 contribution of each relevant regressor. This approach has been used in many previous studies to investigate the relative importance of model predictors in $PM_{2.5}$ concentrations (72), clouds, and changes in radiative forcing (38).

Funding

Supplementary Material

Supplementary Material is available at *PNAS Nexus* online.

Authors' Contributions

Z. Z., X. L., J. C., and H. H. designed research; Z. Z. and J. J. performed research; Z. Z., B. L., and X. M. analyzed data; Z. Z., and X. L. wrote the paper.

Data Availability

All study data are included in the article and Supplementary Material.

References

1. Xiao Q, *et al.* 2021. Tracking PM2.5 and O3 Pollution and the Related Health Burden in China 2013–2020. Environ Sci Technol 56(11): 6922–6932 10.1021/acs.est.1c04548.

2. Turner MC, *et al.* 2016. Long-term Ozone exposure and mortality in a large prospective study. Am J Respir Crit Care Med 193:1134–1142.

3. Haagen-smit AJ, Bradley CE, Fox MM. 1953. Ozone formation in photochemical oxidation of organic substances. Ind Eng Chem 45:2086–2089.

4. Levy IH. 1971. Normal atmosphere: large radical and formaldehyde concentrations predicted. Science 173:141–143.

5. Wang T, *et al.* 2017. Ozone pollution in China: a review of concentrations, meteorological influences, chemical precursors, and effects. Sci Total Environ 575:1582–1596.

6. Kleinman LI. 1994. Low and high NO_x tropospheric photochemistry. J Geophys Res 99:16831–16838.

7. Sillman S. 1999. The relation between ozone, NO_x and hydrocarbons in urban and polluted rural environments. Atmos Environ 33:1821–1845.

8. Jin X, Holloway T. 2015. Spatial and temporal variability of ozone sensitivity over China observed from the Ozone Monitoring Instrument. J Geophys Res Atmospheres 120:7229–7246.

9. Liu H, *et al.* 2018. Ground-level ozone pollution and its health impacts in China. Atmos Environ 173:223–230.

10. Silver B, Reddington CL, Arnold SR, DV. 2018. Spracklen, substantial changes in air pollution across China during 2015–2017. Environ Res Lett 13:114012.

11. Lu X, *et al.* 2018. Severe surface ozone pollution in China: a global perspective. Environ Sci Technol Lett 5:487–494.

12. Xue T, *et al.* 2020. Estimating spatiotemporal variation in ambient ozone exposure during 2013–2017 using a data-fusion model. Environ Sci Technol 54:14877–14888.

13. Wang T, *et al.* 2022. Ground-level ozone pollution in China: a synthesis of recent findings on influencing factors and impacts. Environ Res Lett 17:063003.

14. Ding D, *et al.* 2021. Optimization of a NOx and VOC cooperative control strategy based on clean air benefits. Environ Sci Technol 56:739–749.

15. Pusede SE, Cohen RC. 2012. On the observed response of ozone to NOx and VOC reactivity reductions in San Joaquin Valley California 1995–present. Atmos Chem Phys 12:8323–8339.

16. Roberts SJ, *et al.* 2022. Multidecadal trends in ozone chemistry in the Baltimore-Washington Region. Atmos Environ 285:119239.

17. Bauwens M, *et al.* 2020. Impact of coronavirus outbreak on NO2 pollution assessed using TROPOMI and OMI observations. Geophys Res Lett 44:e2020GL087978.

18. Liu F, *et al.* 2020. Abrupt decline in tropospheric nitrogen dioxide over China after the outbreak of COVID-19. Sci Adv 6:eabc2992.

19. Shi X, Brasseur GP. 2020. The response in air quality to the reduction of Chinese Economic Activities during the COVID-19 outbreak. Geophys Res Lett 47:e2020GL088070.

20. Li L, *et al.* 2020. Air quality changes during the COVID-19 lockdown over the Yangtze River Delta region: an insight into the impact of human activity pattern changes on air pollution variation. Sci Total Environ 732:139282.

21. Tang R, *et al.* 2021. Global air quality change during the COVID-19 pandemic: regionally different ozone pollution responses COVID-19. Atmos Ocean Sci Lett 14:100015.

22. Yin H, *et al.* 2021. Opposite impact of emission reduction during the COVID-19 lockdown period on the surface concentrations of PM2.5 and O3 in Wuhan, China. Environ Pollut 289:117899.

23. Huang X, *et al.* 2021. Enhanced secondary pollution offset reduction of primary emissions during COVID-19 lockdown in China. Natl Sci Rev 8:nwaa137.

24. Sicard P, *et al.* 2020. Amplified ozone pollution in cities during the COVID-19 lockdown. Sci Total Environ 735:139542.

25. Shi Z, *et al.* 2020. Abrupt but smaller than expected changes in surface air quality attributable to COVID-19 lockdowns. Science 369:702–706.

26. Li K, *et al.* 2020. Increases in surface ozone pollution in China from 2013 to 2019: anthropogenic and meteorological influences. Atmos Chem Phys 20:11423–11433.

27. Yang G, Liu Y, Li X. 2020. Spatiotemporal distribution of ground-level ozone in China at a city level. Sci Rep 10:7229.

28. Zhang G, *et al.* 2021. Simultaneous observation of atmospheric peroxyacetyl nitrate and ozone in the megacity of Shanghai, China: regional transport and thermal decomposition. Environ Pollut 274:116570.

29. Li K, *et al.* 2019. A two-pollutant strategy for improving ozone and particulate air quality in China. Nat Geosci 12:906–910.

30. Sun Y, *et al.* 2014. Investigation of the sources and evolution processes of severe haze pollution in Beijing in January 2013. J Geophys Res Atmospheres 119:4380–4398.

31. Lei L, *et al.* 2021. Long-term characterization of aerosol chemistry in cold season from 2013 to 2020 in Beijing, China. Environ Pollut 268:115952.

32. Liu Z, *et al.* 2021. How to apply O3 and PM2.5 collaborative control to practical management in China: A study based on meta-analysis and machine learning. Sci Total Environ 772:145392.

33. Wang H, *et al.* 2022. Seasonality and reduced nitric oxide titration dominated ozone increase during COVID-19 lockdown in eastern China. NPJ Clim Atmos Sci 5:24 .

34. Zhang R, *et al.* 2020. NO_x emission reduction and recovery during COVID-19 in East China. Atmosphere 11:433.

35. Liu T, *et al.* 2020. Driving forces of changes in air quality during the COVID-19 lockdown period in the Yangtze River Delta region, China. Environ Sci Technol Lett 7:779–786.

36. Pu X, *et al.* 2017. Enhanced surface ozone during the heat wave of 2013 in Yangtze River Delta region, China. Sci Total Environ 603–604:807–816.

37. Li M, *et al.* 2021. Large scale control of surface ozone by relative humidity observed during warm seasons in China. Environ Chem Lett 19:3981–3989.

38. Dang R, Liao H, Fu Y. 2021. Quantifying the anthropogenic and meteorological influences on summertime surface ozone in China over 2012-2017. Sci Total Environ 754:142394.

39. Liu Y, *et al.* 2021. Diverse response of surface ozone to COVID-19 lockdown in China. Sci Total Environ 789:147739.

40. Zhao Y, *et al.* 2020. Atmospheric ozone chemistry and control strategies in Hangzhou, China: Application of a 0-D box model. Atmos Res 246:105109.

41. Ma X, *et al.* 2019. Winter photochemistry in Beijing: observation and model simulation of OH and HO_2 radicals at an urban site. Sci Total Environ 685:85–95.

42. Tan Z, *et al.* 2018. Wintertime photochemistry in Beijing: observations of RO_x radical concentrations in the North China Plain during the BEST-ONE campaign. Atmos Chem Phys 18:12391–12411.

43. Wang Y, *et al.* 2021. Enhanced atmospheric oxidation capacity and associated ozone increases during COVID-19 lockdown in the Yangtze River Delta. Sci Total Environ 768:144796.

44. Lu X, *et al.* 2017. Radical budget and ozone chemistry during autumn in the atmosphere of an urban site in central China. J Geophys Res Atmospheres 122:3672–3685.

45. Ivatt PD, Evans MJ, Lewis AC. 2022. Suppression of surface ozone by an aerosol-inhibited photochemical ozone regime. Nat Geosci 15:536–540.

46. Dusanter S, *et al.* 2009. Measurements of OH and HO$_2$ concentrations during the MCMA-2006 field campaign—Part 2: model comparison and radical budget. Atmos Chem Phys 9:1665–1685.

47. Elshorbany YF, *et al.* 2009. Oxidation capacity of the city air of Santiago, Chile. Atmos Chem Phys 9:2257–2273.

48. Chen X, *et al.* 2019. The synergetic control of NO$_2$ and O$_3$ concentrations in a manufacturing city of southern China. Atmos Environ 201:402–416.

49. Lyu X, *et al.* 2019. Causes of a continuous summertime O$_3$ pollution event in Jinan, a central city in the North China Plain. Atmos Chem Phys 19:3025–3042.

50. Wang Y, *et al.* 2018. Surface O$_3$ photochemistry over the South China Sea: application of a near-explicit chemical mechanism box model. Environ Pollut 234:155–166.

51. He Z, *et al.* 2019. Contributions of different anthropogenic volatile organic compound sources to ozone formation at a receptor site in the Pearl River Delta region and its policy implications. Atmos Chem Phys 19:8801–8816.

52. Leung DM, *et al.* 2020. Wintertime particulate matter decrease buffered by unfavorable chemical processes despite emissions reductions in China. Geophys Res Lett 47:e2020GL087721.

53. Lu X, *et al.* 2020. Progress of air pollution control in China and its challenges and opportunities in the ecological civilization era. Engineering 6:1423–1431.

54. Zhu J, *et al.* 2020. Observationally constrained modeling of atmospheric oxidation capacity and photochemical reactivity in Shanghai, China. Atmos Chem Phys 20:1217–1232.

55. Huang X, *et al.* 2017. Chemical characterization and source identification of PM$_{2.5}$ at multiple sites in the Beijing–Tianjin–Hebei region, China. Atmos Chem Phys 17:12941–12962.

56. Guo H, *et al.* 2017. Tropospheric volatile organic compounds in China. Sci Total Environ 574:1021–1043.

57. Gong K, *et al.* 2021. Quantifying the impacts of inter-city transport on air quality in the Yangtze River Delta urban agglomeration, China: implications for regional cooperative controls of PM2.5 and O3. Sci Total Environ 779:146619.

58. Yu Y, *et al.* 2019. Driving factors of the significant increase in surface ozone in the Yangtze River Delta, China, during 2013–2017. Atmos Pollut Res 10:1357–1364.

59. Zhang K, *et al.* 2021. Explicit modeling of isoprene chemical processing in polluted air masses in suburban areas of the Yangtze River Delta region: radical cycling and formation of ozone and formaldehyde. Atmos Chem Phys 21:5905–5917.

60. Zhang K, *et al.* 2021. Formation mechanism of HCHO pollution in the suburban Yangtze River Delta region, China: a box model study and policy implementations. Atmos Environ 267:118755.

61. Zhong J, *et al.* 2021. Robust prediction of hourly PM2.5 from meteorological data using LightGBM. Natl Sci Rev 8:nwaa307.

62. Chen TS, *et al.* 2020. Volatile organic compounds and ozone air pollution in an oil production region in northern China. Atmos Chem Phys 20:7069–7086.

63. Edwards PM, *et al.* 2014. High winter ozone pollution from carbonyl photolysis in an oil and gas basin. Nature 514:351–354.

64. Wang Y, *et al.* 2017. Long-term O$_3$–precursor relationships in Hong Kong: field observation and model simulation. Atmos Chem Phys 17:10919–10935.

65. Zhang K, *et al.* 2021. Explicit modeling of isoprene chemical processing in polluted air masses in suburban areas of the Yangtze River Delta region: radical cycling and formation of ozone and formaldehyde. Atmos Chem Phys 21:5905–5917.

66. Shen HQ, *et al.* 2021. Significance of carbonyl compounds to photochemical ozone formation in a coastal city (Shantou) in eastern China. Sci Total Environ 764:144031.

67. Xue LK, *et al.* 2015. Development of a chlorine chemistry module for the Master Chemical Mechanism. Geosci Model Dev 8:3151–3162.

68. Xue LK, *et al.* 2014. Ground-level ozone in four Chinese cities: precursors, regional transport and heterogeneous processes. Atmos Chem Phys 14:13175–13188.

69. Cardelino CA, Chameides WL. 1995. An observation-based model for analyzing ozone precursor relationships in the urban atmosphere. J Air Waste Manage Assoc 45:161–180.

70. Carter WPL, Atkinson R. 1989. Computer modeling study of incremental hydrocarbon reactivity. Environ Sci Technol 23:864.

71. Carter WPL, Seinfeld JH. 2012. Winter ozone formation and VOC incremental reactivities in the Upper Green River Basin of Wyoming. Atmos Environ 50:255–266.

72. Yang Y, Liao H, Lou S. 2016. Increase in winter haze over eastern China in recent decades: roles of variations in meteorological parameters and anthropogenic emissions. J Geophys Res Atmospheres 121:13,050–013,065.